ARTICLE

Corrosion of Spheroidal Graphite Cast Iron GGG40 in Anoxic Opalinus-Clay Water: Influence of Hydrostatic Pressure

Andrés G. Muñoz[1] | Dieter Schild[2]

[1]Gesellschaft für Anlagen und Reaktorsicherheit GRS gGmbH, Braunschweig, Germany | [2]Institute for Nuclear Waste Disposal, Karlsruhe Institute of Technology, Eggenstein-Leopoldshafen, Germany

Correspondence: Andrés G. Muñoz (andres.munoz@grs.de)

Received: 29 November 2024 | **Accepted:** 6 February 2025

Funding: The German Federal Ministry for the Environment, Nature Conservation, Nuclear Safety and Consumer Protection (BMUV), under project contract 02 E 11981A is expressly acknowledged for the funding of this work.

Keywords: corrosion under pressure | Opalinus-clay water | radioactive waste repositories | spheroidal graphite cast iron steel

ABSTRACT

The corrosion of spheroidal graphite cast iron GGG40 in artificial geological water under anaerobic conditions at 30°C was studied under hydrostatic pressures of 0.5 and 10.0 MPa by electrochemical polarization and impedance spectroscopy. The chemistry and the morphology of the corroded surface were investigated by SEM-EDX and local XPS. High hydrostatic pressures increase the corrosion rate by a simultaneous acceleration of the anodic and cathodic reactions caused by adsorbed atomic hydrogen generated by the water reduction. This activates the anodic dissolution of ferrite and reduces the coverage of poor passivating iron oxides. The release of silicon in the cast iron matrix induces the formation of iron phyllosilicates adhered to the surface.

1 | Introduction

Spheroidal graphite cast iron (GGG 40/EN-GJS-400-15 C) is one of the selected materials for the manufacturing of the overpack of the Pollux 10 container, regarded as a reference for the storage of spent nuclear fuels in different types of host rocks [1]. Bentonite, used as a backfill material becomes the near field environment after the emplacement of containers in granite repositories. After an initial dry phase generated by an intense heat release from the container surface, the bentonite is expected to soak with geological water as the temperature falls under the saturation point [2, 3]. Also, the consumption of enclosed oxygen by reaction with the container wall, microbes, and minerals creates an anoxic atmosphere [4]. The bentonite swelling generates hydrostatic pressures which may exert loads of 5 to 10 MPa depending on the type of bentonite and the depth of the repository [5–7]. The influence of hydrostatic pressure on the corrosion of steels was extensively investigated in the frame of the corrosion of pipelines in deep sea [8–10]. Li et al. [11], for instance, explored the effects of pressure on the corrosion rate of carbon steel X65 using a hydraulic system with aerated artificial see water (3.5 wt% NaCl). The corrosion rate measured by weight loss increased almost linearly by 6.25 $\mu m\, y^{-1}\, MPa^{-1}$. Reported polarizations of steels X70 [12] and X80 [13] indicate that the increase in corrosion rate arises from an acceleration of the anodic reaction. Experimental and theoretical studies on pure iron attribute this effect to a thinning of the outer Helmholtz layer [14, 15]. Hydrostatic pressure, moreover, enhances the rate of the water reduction on Armco iron from 3.5 wt% NaCl solutions [16]. This effect is associated with an increment in the rate of the Heyrovsky step [14–17] caused by an increase in the coverage of atomic hydrogen [16, 17] and the shift of the outer Helmholtz plane towards the surface. Pressure induces a larger permeation of atomic hydrogen into the subsurface and a

[Correction added on 5 March 2025, after first online publication: The affiliation is updated.]

subsequent diffusion to the bulk [16, 17], thus hindering the Tafel step (fusion of two adsorbed hydrogen atoms).

Regarding the covering corrosion products, Li et al. found that Fe_3O_4 predominates over γ-FeOOH and α-Fe_2O_3 after the corrosion of steel X65 under 12 MPa pressure in seawater, whereas mainly γ-FeOOH is found at atmospheric pressure [11]. This diverges from other works reporting only 3% of Fe_3O_4 formed under 10 MPa on X80 [13] or a decrease of Fe_3O_4 from 50% to 26% on low alloy steel [10] as the pressure increased from 0.1 to 3.5 MPa. The compositional differences may arise due to different initial contents of dissolved oxygen in the experiments [18]. Under anoxic conditions, γ-FeOOH (lepidocrocite) and $Fe(OH)_2$ may appear as the first oxidation products in light alkaline solutions [19]. Their evolution to the more stable magnetite (Fe_3O_4) is constrained by the reaction kinetics.

The model experiments presented in this paper aim to analyze the influence of hydrostatic pressure on the corrosion mechanism of spheroidal graphite cast iron in anoxic artificial geological water, reproducing in part the conditions expected in a repository.

2 | Materials and Methods

2.1 | Electrochemical Measurements

Polarizations and electrochemical impedance measurements were performed with a high-pressure, high-temperature stainless steel reactor manufactured by Berghof Products & Instruments GmbH, Germany (see Figure 1). The reaction vessel was lined with a Teflon capsule. The temperature was set by an electric heater and controlled by a thermocouple inside the reactor. The cell was pressurized with nitrogen. High-temperature, high-pressure reference, counter and working electrodes with a body of titanium were purchased from Corr Instruments, San Antonio, Texas. An ambient temperature Ag/AgCl (3 M NaCl) electrode (out of reactor) was used as a reference. Potentials in the text are referred to as this electrode. The electrodes were inserted into the reactor by appropriate sealing screws. Electrochemical runs were carried out with a Solartron electrochemical interface 1287 A coupled to a frequency analyzer 1260 A commanded with CorrWare and ZPlot/ZView software.

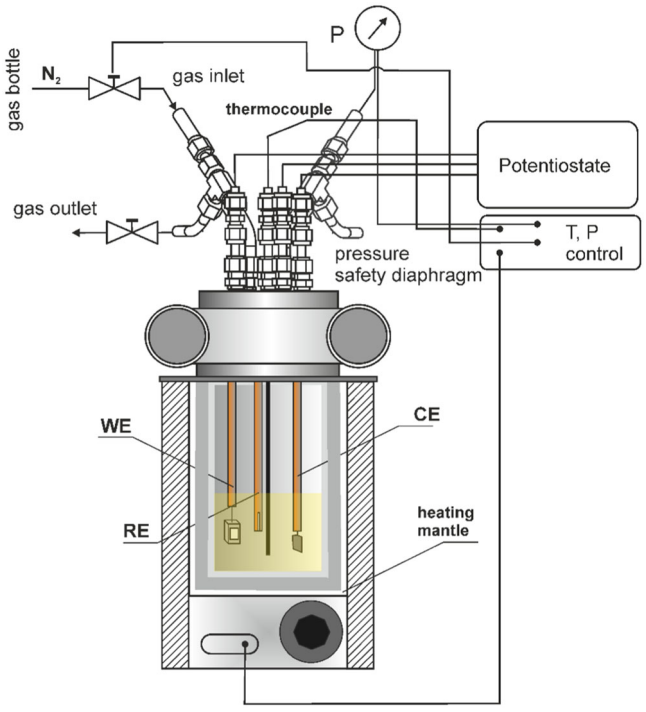

FIGURE 1 | Schematic representation of the H-P/H-T cell. [Color figure can be viewed at wileyonlinelibrary.com]

2.2 | Materials and Electrolyte

Samples are 6 × 6 × 4 mm pieces of cast iron GGG40 were embedded in Araldite†. The exposed face was successively polished with emery paper up to grade 1000 and diamond suspensions of 6 and 1 μm. The samples were sonicated successively in isopropanol, acetone, ethanol, and pure water and dried under argon stream before their mounting in the reactor. The composition of the steel is given in Table 1. The test electrolyte was Opalinus Clay water type A (see composition in Table 2), prepared using analytical grade chemicals and ultrapure water (18.2 MΩ.cm Milli-Q system, Millipore). The solution was deaerated by purging Ar before the experiment. After experiments, the samples were rinsed with degassed ultrapure water, dried under Ar stream, and immediately stored in an argon glovebox for their surface analysis.

2.3 | Surface Analysis

For XPS analyses, air-sensitive samples from electrochemical experiments were mounted under anoxic conditions on a sample holder and transferred into the analysis chamber of the XPS equipment using a gas-tight transfer vessel. XPS spectra were recorded with a PHI 5000 VersaProbe II system (ULVAC-PHI Inc). It is equipped with a scanning microprobe X-ray source (monochromatic Al Kα 1486.7 eV) in combination with an electron flood gun and a floating ion gun generating low energy electrons (1 eV) and low energy argon ions (6 eV) for charge compensation of isolating samples (dual beam technique). The base pressure inside the spectrometer was about 2×10^{-7} Pa. The angle between the sample surface and the analyzer was set to 45°. Survey scans were recorded with a pass energy of 187.85 eV of the analyzer and X-ray beam spot sizes 200 μm of diameter at X-ray source power 30 W. In case of small sample features, scanning X-ray imaging (SXI) with an X-ray spot size of 5 μm was applied to define the positions of analysis areas. Survey scans were used to identify the elements and to determine their relative atomic concentrations (except hydrogen) by areas of elemental lines after Shirley background subtraction, elemental sensitivity factors, asymmetry parameters, and transmission function of the analyzer. The relative error of atomic concentrations is expected to be within ± (10%–20%). Data analysis was performed using ULVAC-PHI MultiPak program, version 9.9.3. A scanning electron microscope (FEI Quanta 650 FEG) equipped with a silicon drift EDS detector (Thermo Scientific, Noran System 7) was used for imaging and X-ray microanalysis by Pathfinder software ver. 2.11 of sample surfaces.

TABLE 1 | Nominal chemical composition of GGG40 steel.

Element	C	Si	Mn	P	S	Mg	Cr	Cu	Fe
%at	13.85	5.80	0.25	0.14	0.004	0.10	0.039	0.028	79.86

TABLE 2 | Elemental chemical composition of Opalinus-clay water type A/pH 7.6.

Element	Na	Cl	K	Mg	Ca	Sr	SO_4	HCO_3
mol kg^{-1}	0.24	0.30	0.0016	0.017	0.026	0.00065	0.014	0.00048

Core-level photoelectron spectra were deconvoluted using the software UNIFIT 2019. The convolution of Lorentzian and Gaussian functions (Voigt profile) was used for the modeling of the peak shapes. The calculation of the background was included in the fitting procedure using a universal background description for inhomogeneous samples. This includes a polynomial component, Bp (E) = a + b E + c E2 + d E3 which represents the secondary electron background, a Shirley component: BS(E) = e S(E) and an improved Tougaard background component using a five-parameter inelastic electron scattering cross section: B, C, C′, D and T0 [20]. The intensity ratio of spin-orbit double peaks and their energy separation were fixed.

3 | Results

3.1 | Electrochemical Studies

Figure 2 shows the current-voltage curves of GGG40 in Opalinus Clay water run after being 48 h at the corrosion potential for different pressures. An almost flat cathodic current can be observed for 0 MPa overpressure. The anodic part increases exponentially, as expected for a kinetically controlled iron dissolution. The increase of hydrostatic pressure to 0.5 MPa generated by nitrogen injection in the reactor brings about an increase of the cathodic current and the onset of an exponential course at the cathodic limit. This effect is enhanced by increasing the pressure to 10 MPa. It is interesting to note that the increase of hydrostatic pressure also induces random current oscillations with an amplitude of about 10 μA for 0.5 MPa. The fluctuations reduce to 2 μA at 10 MPa. Figure 3 shows the mean current of curves shown in (a) plotted as log |I| vs potential. The diagrams show a change of the anodic slope of the dissolution of iron from 62.5 mV dec^{-1} under 0 MPa to 34 mV dec^{-1} at 0.5 MPa bar and further to 26 mV dec^{-1} at 10 MPa. Moreover, the corrosion potential shifts from −0.75 V at 0 MPa to −0.705 V at 0.5 MPa and to −0.68 V at 10 MPa. The corresponding corrosion currents are 0.28, 0.75, and 2.8 μA for 0, 0.5, and 10 MPa respectively.

Nyquist plots of GGG40 obtained at the corrosion potential after 48 h are shown in Figure 4 for 0.5 and 10 MPa. In both cases, the high-frequency region is characterized by a capacitive loop attributable to the double-layer capacitance and the interfacial charge transfer. This former changes from 55.4 μF cm^{-2} at 0.5 MPa to 13.8 μF cm^{-2} at 10 MPa. The charge transfer resistance, however, changes from 59.6 to 68.4 Ω cm^2. Thus, the change of capacitance should rather reflect a change of the chemical nature of the interface rather than a change of the active area. The low-frequency inductive and capacitive behaviors at 0.5 and 10 MPa, respectively, reflect the dynamics of the reaction steps involving adsorbed species, as discussed below.

3.2 | Surface Morphological and Chemical Studies

3.2.1 | SEM-EDX Studies

Figure 5 shows representative micrographs of the GGG40 surface after 48 h corrosion at 30°C in Opalinus Clay water at 0.5 MPa (a–c) and 10 MPa (d–f). At 0.5 MPa, the corroded surface presents a preferential attack around the graphite spheres (a). Some of them have been loosed leaving a cavity with a crystallographic aspect free of precipitates. A closer examination of the surface corroded at 0.5 MPa around the graphite spheres (b) identifies the different metallographic phases of the cast iron, e.g., feather-like, and grains with a flat appearance. The formers arise from the selective dissolution of ferrite lamellae in the dominating pearlitic matrix. The latter, with an EDX-determined composition of 86.1 at% Fe and 11.6 at% C (point 1 in b), can be assigned to ledeburite. Two types of morphologies predominate in the corrosion products: thin polyhedral platelets combined with aggregates of small grains of a geometrical aspect. EDX performed at area 2 of Figure 5b indicates a composition: 15 at% C, 39.2 at% O, 2.6 at% Al, 5,1 at% Si and 37.6 at% Fe. The EDX analysis of area 3 indicates rather lower C and Si contents but a large oxygen content: 8.5 at% C, 57.2 at% O, 3.1 at% Si and 28.8 at% Fe. Figure 5c shows an enlargement of one of the precipitates set on the surface of a graphite nodule. EDX analysis performed on area 4, gives a composition: 49.3 at% C, 36,6 at% O, 3.3 at% Si and 9.7 at% Fe. The large carbon content indicates that the EDX signal captures a considerable fraction of the substrate composition, which should be considered by the characterization of the precipitates.

After corrosion at 10 MPa, the surface shows a similar morphological aspect but without the presence of precipitates on the surface (Figure 5d). The fine hair-like structure of the corroded matrix (see Figure 5e) indicates a substantial ingoing attack. The attack embraces the dissolution of the ledeburite structure leaving circular shaped holes on the flat structures (see Figure 5e). Figure 5f shows a more detailed picture of the hair-like structure left after the matrix dissolution. This type of attack suggests an acceleration of the dissolution of the ferrite lamellae of the pearlite structure induced by inward diffusion of hydrogen.

Figure 6 shows an EDX-mapping of the surface after corrosion at 10 MPa. Essentially, six compositional phases with elemental

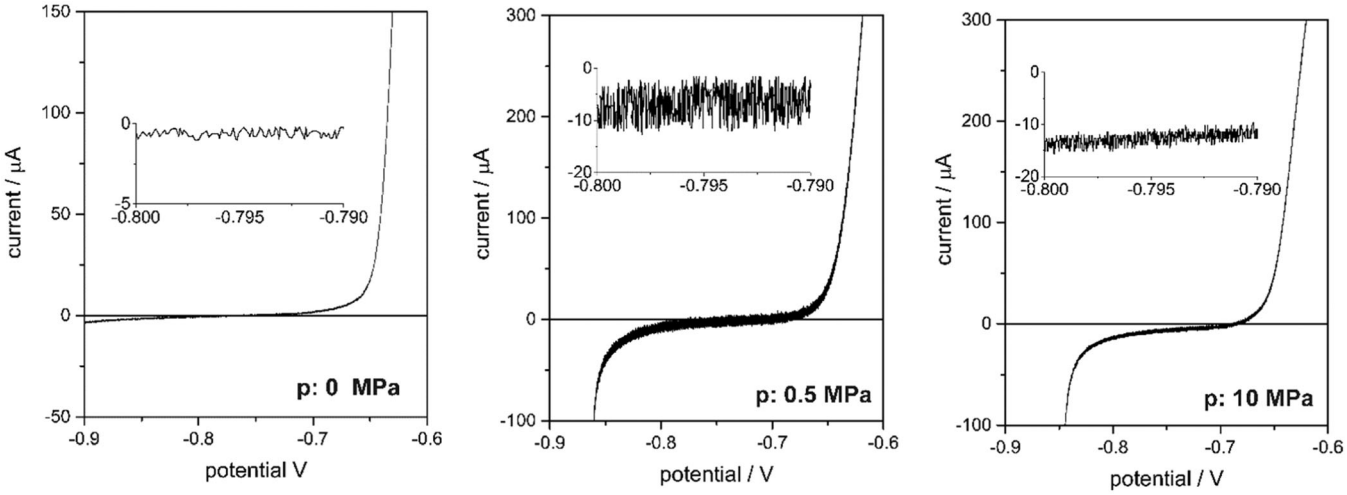

FIGURE 2 | Polarization curves of GGG40 in Opalinus Clay water at 30°C and different pressures after 48 h at the corrosion potential. Scan rate: 0.166 mV s^{-1}. V_{ic}: −0.10 V vs OCP.

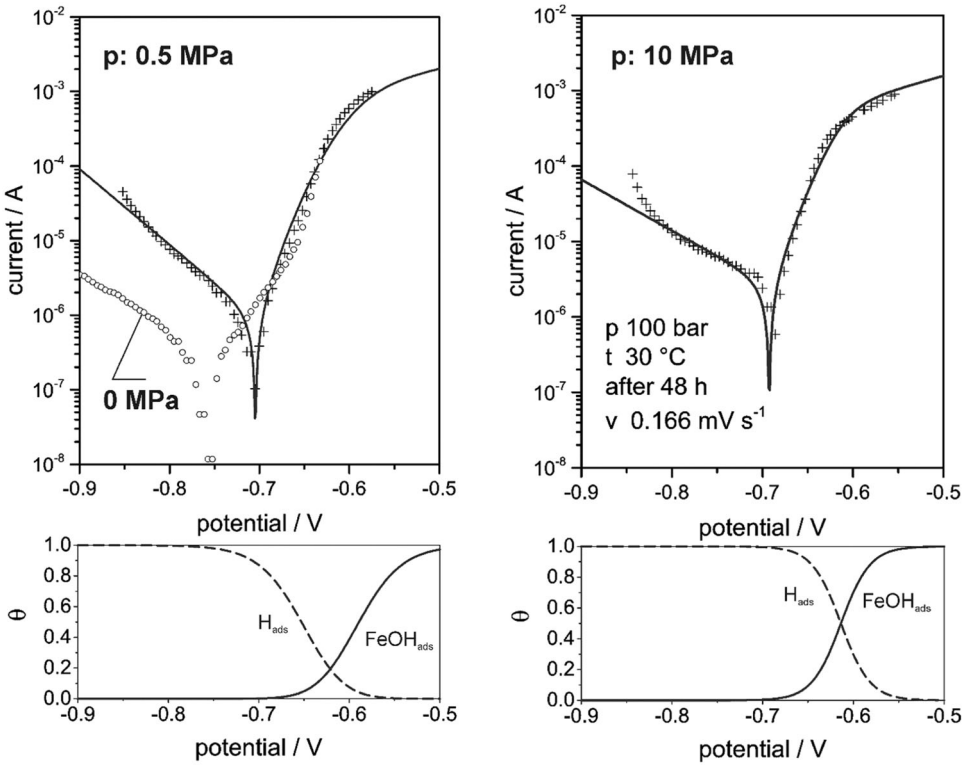

FIGURE 3 | Polarization curves of GGG40 in Opalinus Clay water at 30°C and different hydrostatic pressures. Points: mean current values of the current-voltage curves of GGG40 in represented as log |I| vs V. Solid lines: calculated polarization curves and surface coverages of adsorbed intermediary species.

distributions as given in Table 3 could be identified by applying the direct-to-phase analysis tool provided by the EDX analysis software. This latter combines a chi-squared-based spectrum match with a multi-variant statistical and correlation analysis of the spectral imaging. The matrix is mainly characterized by phase *a* with a Fe:C ratio of about 6. The phases *e* and *f* follow the same pattern as phase *a* but are characterized by ratios Fe:C of 3.4 and 4.0 and ratios Fe:O of 3.0 and 5.2, respectively. These compositions arise from the preferential dissolution of ferrite lamellae in the pearlite structure. The phase *c*, appearing around the still attached graphite spheres and on the semispherical cavities left after the detachment of some of them is characterized by a Fe:C ratio of 21.0. This suggests that this phase corresponds to the preferentially corroded ferrite. The phase *d* appears at the periphery of the ferrite cavities left after the release of the graphite spheres. It is characterized by a large content of O and Si, indicating the presence of iron silicates attached to the surface. Apart from this phase, the O < 20 at% in the other phases, points out a surface practically free of surface oxides. Silicon, as a ferrite stabilizing element [21] is expected to accumulate around the graphite spheres [22, 23]. The white-appearing dendrites embracing dark-appearing dots and rods

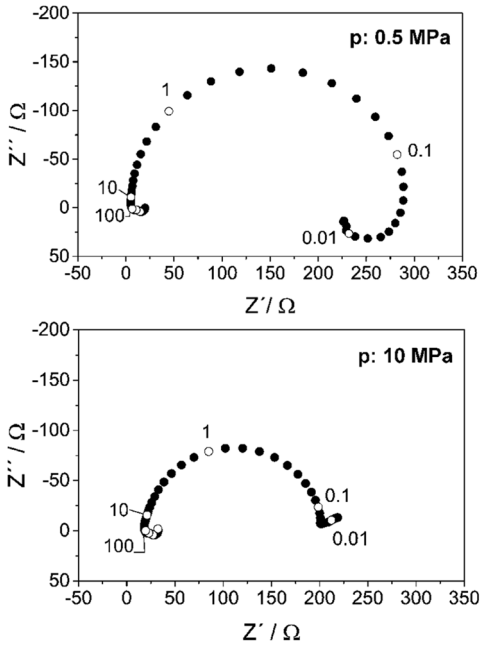

FIGURE 4 | Nyquist plots of GGG40 in Opalinus Clay water at 30°C and different hydrostatic pressures. Frequencies indicated in Hz.

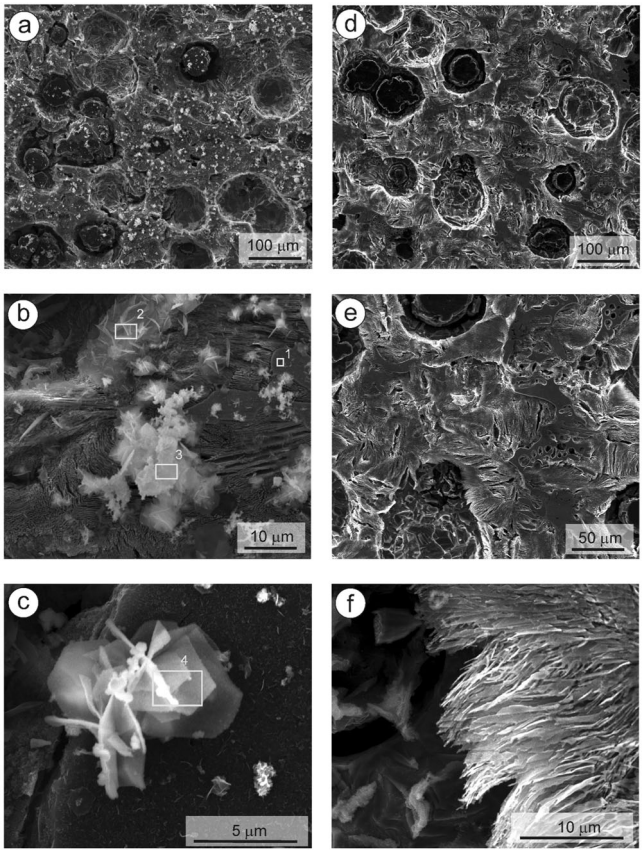

FIGURE 5 | Secondary electron images of GGG40 after 48 h corrosion in Opalinus Clay water at 30°C under hydrostatic pressures of 0.5 MPa (a–c) and 10 MPa (d–f). Squares indicate the position of local EDX analysis (see text).

(see feature marked with a dashed line in a and c) can be attributed to ledeburite with round islands of pearlite arising from the eutectic transformation of austenite. The ledeburite dendrite matches with an intense signal of phase *a*, whereas the dark spots match with phase *c*.

3.2.2 | Photoelectron Spectroscopy

Figure 7 shows the Fe2p core level spectra measured on cast iron after 48 h corrosion in Opalinus Clay water at 0.5 and 10 MPa. A classical spectra deconvolution in lines corresponding to Fe(0), Fe(II), and Fe(III) using Voigt functions was performed. It can be shown that the Voigt functions represent quite reasonably the envelope of the fine structure described by the Gupta-Sen splitting concept [24, 25]. The lines Fe(0), Fe(II), and Fe(III) appear at 706.7, 710.6 and 712.8 eV for 0.5 MPa and 706.7 eV, 710.6 and 713.0 eV for 10 MPa. The chemical shifts of satellites (II) and (III) are +5.3 eV and +6.6 eV and +6.3 eV and +6.9 eV for 0.5 MPa and 10 MPa respectively.

The intensity ratio Fe(II)/Fe(III) was found 1.1 and 1.2 for 0.5 and 10 MPa, indicating a common surface chemistry during dissolution. The appearance of the metal signal indicates an incomplete surface coverage or that the oxide film is thinner than the effective attenuation length estimated by 1.1 nm for lepidocrocite [26]. Especially remarkable in both spectra are the large satellite signals, with maximum intensities of about ⅓ to ½ of the main peak in comparison with ratios < ¼ for iron oxide standards [25]. As addressed by Grosvenor et al. [25], the satellite peaks increase with decreasing electronegativity of the ligand in FeX_2 compounds (X: Cl, Br, F), whereas there is an almost linear relationship of the ligand electronegativity with the chemical shift of the satellites from the corresponding main Fe(II) and Fe(III) lines. To find the position of −OH ligands in this sequence, we calculated the partial charge of the Fe(II) in FeX_2, δ^+, applying the Sanderson electronegativity concept [27, 28]. Values of $\delta^+ = 0.46$, 0.53 and 0.66 for X: Br, Cl and F respectively can be calculated. Thus, the ligand OH^-, for which $\delta^+ = 0.53$ was calculated, is expected to yield a chemical shift similar to that for Cl^-.

The O1s core level spectra obtained after corrosion in 0.5 and 10 MPa are shown in Figure 8. They could be deconvoluted in 3 lines at 529.8 eV (529.7), 531.4 eV (531.3) and 533.5 eV (533.2) for 0.5 MPa (10 MPa). Line I can be ascribed to O atoms in oxides [29]. The binding energy of line II is close to that of OH^- groups in FeOOH [29, 30]. Oxygen in silicates, such as fayalite [31–33] or phyllosilicates [34] also appears close to this binding energy. But it would be more creditable to ascribe this line to Fe-O-Si bonds. Although line III can be ascribed to water, it is more feasible to assign it to SiO_2 [29, 31].

The intensity ratio of (I_{II}/I_I) changes from 3.8 at 0.5 MPa to 2.2 at 10 MPa, whereas the ratio $I_{III}/(I_{II} + I_I)$ decreases from 0.14 to 0.04, respectively.

The Si2p core level spectra after the corrosion experiments are also shown in Figure 8. At 0.5 MPa, the spectrum can be deconvoluted in three lines at 100.4, 102.3, and 103.9 eV. The line I can be ascribed to SiC. The predominating line II is

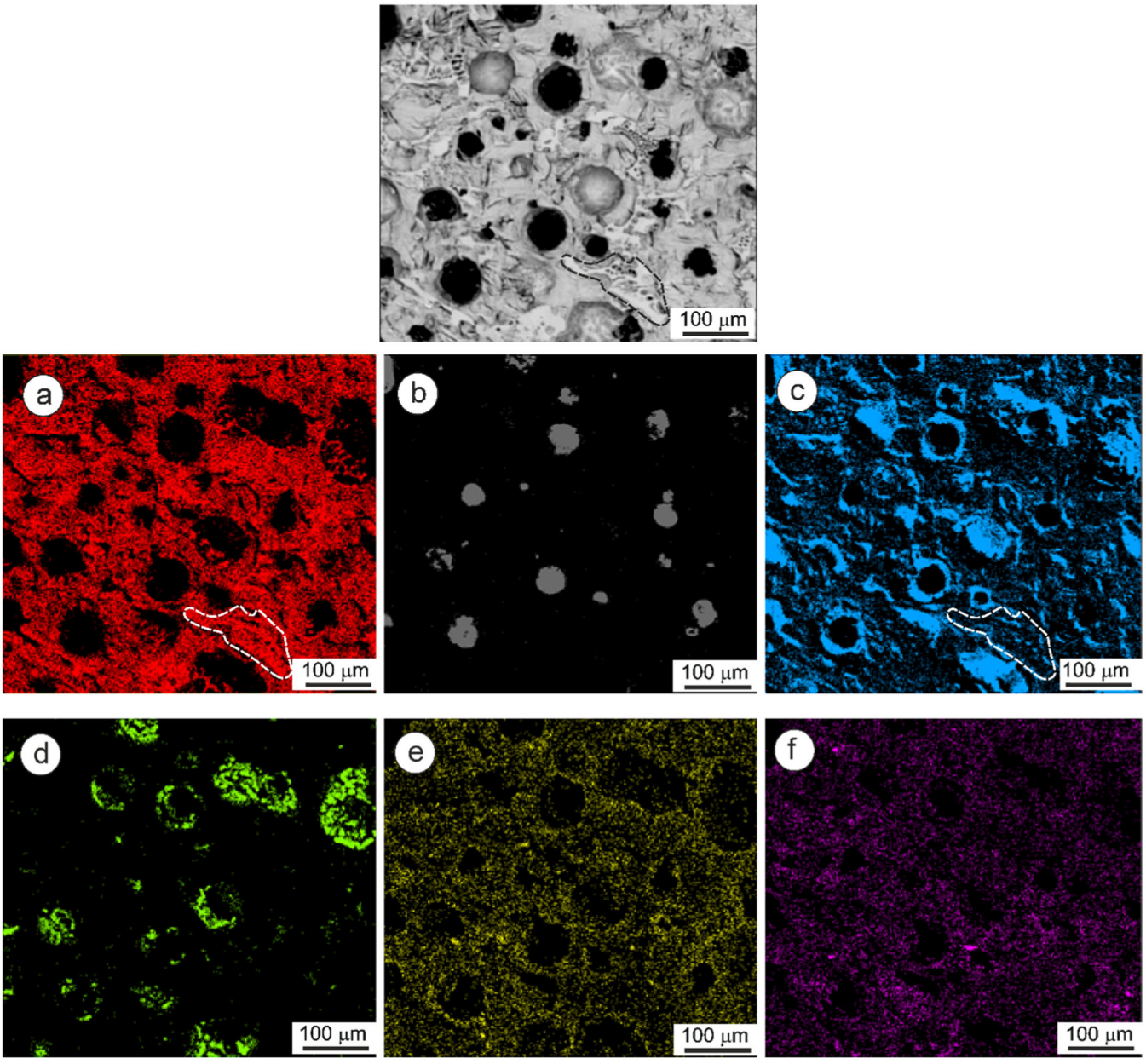

FIGURE 6 | EDX-mapping of the surface of GGG40 after 48 h corrosion at 30°C in Opalinus Clay water at 10 MPa. (a–f) Compositional phases as indicated in Table 3. [Color figure can be viewed at wileyonlinelibrary.com]

TABLE 3 | Elemental composition (at%) of different surface phases identified by EDX in GGG40 after 48 h corrosion in Opalinus Clay water at 30°C and 100 bar.

Element		C	Si	Fe	O	Mn	Al	Cu	Zr
Phase	a	13.9	1.7	82.6	—	0.7	0.2	0.1	0.1
	b	95.5	0.6	3.3	—	—	0.3	0.1	—
	c	8.1	1.6	82.5	5.3	0.8	0.2	0.3	—
	d	18.4	12.0	34.7	29.6	0.1	1.8	1.2	1.0
	e	17.4	0.3	58.9	19.9	0.9	1.0	—	
	f	15.5	1.7	62.2	11.8	1.4	—	0.9	

characteristic of silicates, whereas line III corresponds to SiO_2. At 10 MPa, the signal is reduced to a main line at 102 eV, indicating the presence of silicates and a minor line at 99.01 eV, indicating the presence of Si (0).

The elemental quantification from the survey at 0.5 MPa spectra indicates: 48.3 at% O, 7.7 at% Si and 18.7 at% Fe and 0.5 at% Mg. Following the analysis of the corresponding core level spectra we have: 5 at% Si (silicate), 2.2 at% Si (SiO_2), 8.9 at% O (oxide),

33.6 at% O (line II), 5.8 at% O (SiO_2) 9.7 at% Fe(II) and 9.0 at% Fe(III).

For 10 MPa we have: 42.9 at% O, 3.0 at% Si, and 20.4 at% Fe and 1.5 at% Mg. Thus, 2.7% Si (silicate), 12.9 at% O (oxide), 28.2 at% O (line II), 1.8 at% O (SiO_2), 11.2 at% Fe(II), 9.2 at% Fe(III).

Figure 9 contrasts the valence band spectra after corrosion at 0.5 and 10 MPa with those of different iron oxides obtained from the literature [35]. The spectrum at 0.5 MPa presents four features at 0.32, 2.6, 4.9, and 6.9 eV. Feature I can be ascribed to iron metal. Features II and III can be associated with those appearing in γ-FeOOH. The shoulder IV reflects the contribution of Fe(II)-sites represented by the spectrum of FeO. The larger contribution of the metal signal for 10 MPa shifts upwards feature II. The extrapolation of the rising part of the oxide spectrum to zero intensity indicates the approximated position of the valence band edge of the oxide film respective of the Fermi level. Values of 0.7 and 0.3 eV can be measured for 0.5 and 10 MPa respectively. The different positions of the valence band edges can be related to the different amounts of silicon found in the film. The reference valence band spectra in ref [35]. are presented with an alignment of the valence-band edge to the Fermi level.

4 | Discussion

The polarization curves indicate that the corrosion rate of graphitic cast iron is defined by an active anodic dissolution which is cathodically limited by the water reduction reaction. This later occurs in two electron transfer steps [36]. The first step, the Volmer reaction (1) generates adsorbed atomic H_{ads}. The evolution of molecular hydrogen may occur by a proton discharge on H_{ads}, the Heyrovsky step (2), or by condensation of two H_{ads}, the Tafel step (3).

$$H_2O + e^- + M \underset{k1^-}{\overset{k1^+}{\rightleftarrows}} M - H_{ads} + OH^- \quad (1)$$

$$M - H_{ads} + H_2O + e^- \underset{k2^-}{\overset{k2^+}{\rightleftarrows}} H_2 + M + OH^- \quad (2)$$

$$2\,M - H_{ads} \underset{k3^-}{\overset{k3^+}{\rightleftarrows}} H_2 + 2\,M \quad (3)$$

The mechanism of the active anodic dissolution of iron from the cast iron matrix, on the other hand, involves adsorbed $FeOH_{ads}$ species [37, 38]:

$$Fe + H_2O \underset{k4^-}{\overset{k4^+}{\rightleftarrows}} Fe(H_2O)_{ads} \quad (4)$$

$$Fe(H_2O)_{ads} \underset{k5^-}{\overset{k5^+}{\rightleftarrows}} Fe(OH)_{ads} + e^- + H^+ \quad (5)$$

$$Fe(OH)_{ads} \underset{k6^-}{\overset{k6^+}{\rightleftarrows}} FeOH^+(aq) + e^- \quad (6)$$

Reactions (1), (4), and (5) are supposed to be in equilibrium. Reactions (2) and (6) are the rate-determining steps. $k_{j^\pm}$ are the electrochemical rate constants given by the Butler-Volmer expression:

$$k_{j^\pm} = k_{0j^\pm} \exp[\pm\alpha_{j^\pm}(F/RT)V] \quad (7)$$

where $\alpha_{j^-} = (1 - \alpha_{j^+})$ and $\alpha_{j^+} > 0$ or $\alpha_{j^+} < 0$ for anodic or cathodic reactions respectively.

Under the assumption $k_{2^+} >> k_{3^+}$, $k_{4^+} \approx k_{4^-} >> k_{5^+} \approx k_{5^-}$ the coverage fractions of FeOH (θ_{FeOH}) and Fe—H (θ_H) under steady-state conditions are given by

$$(d\theta_{FeOH}/dt) = k_{5^+}(1 - \theta_{FeOH} - \theta_H) - k_{5^-}\theta_{FeOH}[H^+] - k_{6^+}\theta_{FeOH} = 0 \quad (8)$$

$$(d\theta_H/dt) = k_{1^+}(1 - \theta_{FeOH} - \theta_H) - k_{1^-}\theta_H[OH^-] - k_{2^+}\theta_H = 0 \quad (9)$$

From Equations (8) and (9) we have

$$\theta_{FeOH} = [k_{5^+} - k_{5^+}k_{1^+}/S_1]/[S_2 - k_{5^+}k_{1^+}/S_1] \quad (10)$$

$$\theta_H = k_{1^+}(1 - \theta_{FeOH})/S_1 \quad (11)$$

where $S_1 = (k_{1^+} + k_{1^-}[OH^-] + k_{2^+})$, $S_2 = (k_{5^+} + k_{5^-}[H^+] + k_{6^+})$. The anodic and cathodic currents are then given by

$$I_a = 2Fk_6^+\theta_{FeOH}A \quad (12)$$

$$I_c = 2\,F\,k_2^+\,\theta_H\,A \quad (13)$$

where A is the electrode area. The solid line in Figure 3 shows the results of the model for the parameters indicated in Table A1 of the appendix. The model indicates an increase in the coverage of H_{ads} with pressure. At 10 MPa, there is a displacement of H_{ads} by $FeOH_{ads}$. The polarization curves agree with a predominance of the Volmer–Heyrovsky mechanism. A similar result was addressed by Xiong et al. [14] for the low-carbon steel A514. Our simulated curves presuppose a strong inhibition of the reverse Volmer step (k_{01^-}) and an increase of the rate of the Heyrovsky step (k_{02^+}) by a factor of 500. This can be explained by a closer approach of interfacial water molecules against the metal surface on pressuring, which in turn causes a decrease of α_{2^+} and α_{6^+} [14–16]. Hydrostatic pressure induces the diffusion of adsorbed hydrogen atoms towards the metal subsurface, thus hindering their recombination (Tafel step). Modiano et al. [39] have found that the hydrogen permeation in pure iron during its galvanostatic cathodic conditioning in borate buffer (pH 8.4) reduces the native oxide and brings about an anodic activation. Their XANES measurements have also shown that the dissolution occurs under a thin film of Fe(II) oxide, to which the inductive loop of impedance spectra was ascribed. The appearance of an inductive loop in the impedance diagram performed at 0.5 MPa (see Figure 4a) is evidence that an oxide film is formed at the interface. The anodic activation is linked with a weakening of the iron crystal structure leading to its disintegration after prolonged cathodic hydrogen permeation [40, 41]. In pearlitic structures, atomic hydrogen was found to diffuse in the ferrite lamellae reducing the energy for dislocation motion. This softens ferrite, degrading its mechanical

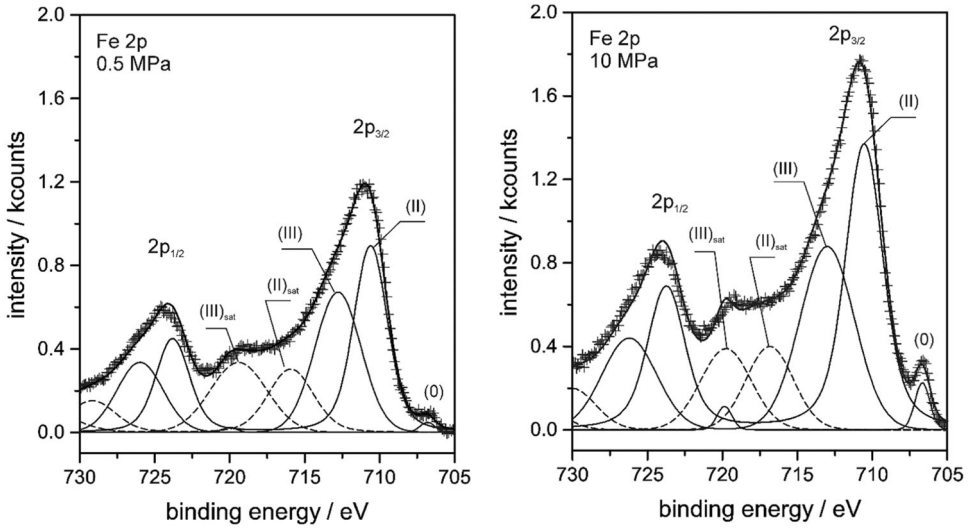

FIGURE 7 | Core level X-ray photoelectron Fe 2p spectra of GGG40 after 48 h corrosion in Opalinus Clay water at 30°C under 0.5 and 10 MPa.

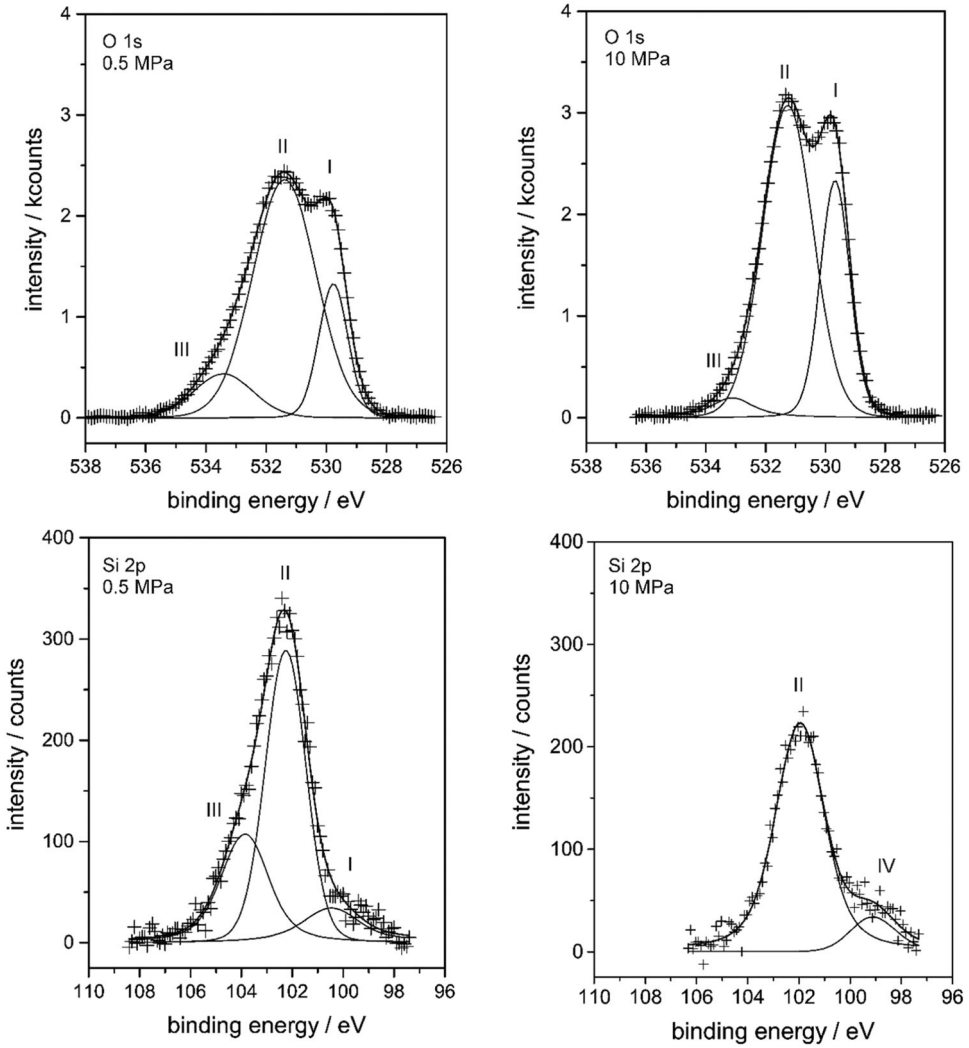

FIGURE 8 | Core level X-ray photoelectron O 1 s and Si 2p spectra of GGG40 after 48 h corrosion in Opalinus Clay water at 30°C under 0.5 and 10 MPa.

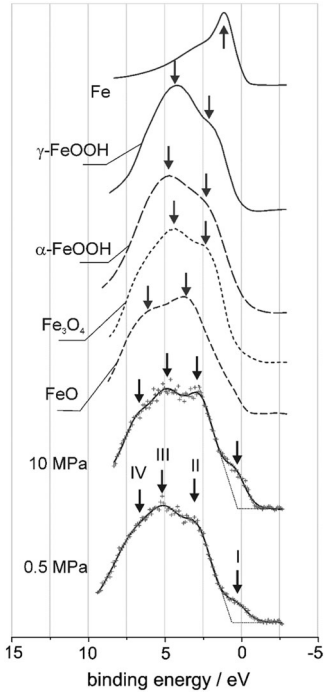

FIGURE 9 | Valence band X-ray photoelectron spectra of GGG40 after 48 h corrosion in Opalinus Clay water at 30°C under 0.5 and 10 MPa compared with reference spectra for different iron oxides.

properties [42]. With a free energy of formation of +27.0 kJ mol^{-1} [43], the anodic dissolution of cementite is thermodynamically unfavorable in comparison with ferrite. Also, the active dissolution rate of Fe_3C was found to be lower than that of ferrite [44]. The preferential dissolution of ferrite is reflected in the undermining of graphite spheres and exposition of comb-like structures by ferrite dissolution of the pearlite matrix. Pressure enhances these effects as shown in Figure 5 with the notary deeper attack of perlite caused by the activation of ferrite by inward diffusion of hydrogen. Adsorbed hydrogen is also expected to reduce the corrosion products at the interface towards soluble Fe(II) species. This is reflected in the fourfold iron metal signal at 10 MPa compared with that at 0.5 MPa.

The chemical thermodynamics of iron, shown in the form of Pourbaix diagram in Figure 10 for normal pressure, predicts the formation of metastable γ-FeOOH and $Fe(OH)_2$ [45, 46]. Whereas magnetite (Fe_3O_4) and fayalite (Fe_2SiO_4) constitute the most stable phases. The potential-pH coordinates for iron corrosion in Opalinus Clay water, as indicated in the diagram, is dominated by the hydrogen evolution reaction. It can be also inferred that the primary products of iron dissolution are $Fe(OH)_2$ and γ-FeOOH. According to Jolivet et al. [47, 48], the layered structures of γ-FeOOH (lepidocrocite) or δ-FeOOH (feroxyhyte) can be only formed by oxidation of the layered brucite-type structure of $Fe(OH)_2$ arising from the condensation of the coordination octahedrons $Fe(OH)_2(H_2O)_4$. Regarding the Gibbs free energy of formation for δ-FeOOH and freshly precipitated $Fe(OH)_2$ of −478.1 kJ mol^{-1} [49] and −490.0 kJ mol^{-1} [50] respectively, it is possible to calculate the standard reduction potential for reaction (14), $V^0 = -0.559$ V (vs Ag/AgCl, 3 M NaCl) at pH 8.

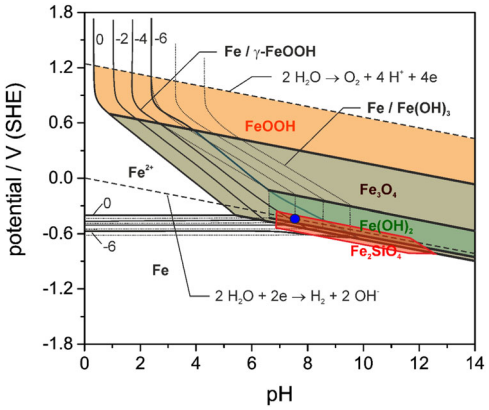

FIGURE 10 | Pourbaix diagram for the systems Fe-Si-H_2O at 25°C. The point represents the thermodynamic description of the corrosion process on ferrite. [Color figure can be viewed at wileyonlinelibrary.com]

$$\delta\text{-FeOOH} + e + H_2O \rightleftarrows Fe(OH)_2 + OH^- \qquad (14)$$

These products are likely to condensate to give magnetite:

$$2\,\delta\text{-FeOOH} + Fe(OH)_2 \rightleftarrows Fe_3O_4 + 2\,H_2O \qquad (15)$$

This is in line with the coexistence of Fe(II) and Fe(III) indicated by the Fe2p core level lines in Figure 7 and the valence band spectra in Figure 9. The deconvolution of the Si2p core level signal in Figure 8 has shown that the main line at 102.2 eV for the relatively large amount of Si (as quantified with the survey spectrum) can be mainly assigned to Si-O-Fe bonds as found in layered silicates [51, 52] or in fayalite [32]. Thus, it appears more feasible that a thin surface layer of iron silicate rather than a mixture of different oxides is formed during iron dissolution. It was reported that the coprecipitation of SiO_2 and $Fe(OH)_2$ at pH > 8 yields layers of polymerized $Fe(OH)_2$ which work as templates for the formation of layered silicates [53]. Thus, local structures like those of greenalite appear. This would better suit with the presence of Si2p lines at 102.2 eV and O1s at 531.5 eV, characteristic for phyllosilicates [52]. In addition, the inherent Fe(II,III)-OH bonds in phyllosilicates should be in agreement with the large satellite lines in the Fe 2p core level spectra (Figure 7). Włodarczyk et al. [54] provided clear evidence of the reactivity of Fe deposited on silica films yielding a silicate monolayer resembling the nontronite structure, with an O1s line at 531 eV assigned to Fe-O-Si bonds. The formation of reduced nontronite structures with Fe(II)/Fe(III) ratios of 1.1 to 1.2, as quantified by the Fe2p signal may be the result of structure-supported redox activity presented by these silicates [55].

5 | Conclusions

The anoxic corrosion of spheroidal graphite cast iron GGG40 in Opalinus Clay water under hydrostatic pressures higher than 0.5 MPa occurs under a kinetically controlled anodic dissolution of ferrite regulated by water reduction. The increase of hydrostatic pressure over 0.5 MPa accelerates the Volmer step of the water reduction increasing the coverage of atomic hydrogen and thus its inward diffusion. Absorbed hydrogen, in turn, enhances the dissolution of iron by weakening its crystal structure. Hydrogen reduces the amount of precipitated iron

oxides in favor of the formation of more stable thin silicate layers. The interfacial reaction mechanism is not completely understood. It is however feasible, that the interfacial alkalization induced by the water reduction leads to a local precipitation of layered $Fe(OH)_2$ and FeOOH as precursors that condensate to phyllosilicate-like structures in the presence of silicon released from the iron matrix in the form of silica.

Author Contributions

A. G. M. was involved in conceptualization, investigation, writing original draft, and project management. D. S. was involved in investigation, review and editing.

Acknowledgments

The German Federal Ministry for the Environment, Nature Conservation, Nuclear Safety and Consumer Protection (BMUV), under project contract 02 E 11981A is expressly acknowledged for the funding of this work.

Conflicts of Interest

The authors declare no conflicts of interest.

Data Availability Statement

The data that support the findings of this study are available from the corresponding author upon reasonable request.

References

1. T. Hassel, A. Köhler, and Ö. S. Kurt, *Das ENCON-Behälterkonzept – Generische Behältermodelle zur Einlagerung radioaktiver Reststoffe für den interdisziplinären Optionsvergleich*, ENTRIA-Arbeitsbericht-16, Institut für Werkstoffe, Leibniz-Universität Hannover, Hannover, Germany, 2019, 2367–3540.

2. D. Landolt, A. Davenport, J. Payer, and D. Shoesmith, *A Review of Materials and Corrosion Issues Regarding Canisters for Disposal of Spent Fuel and High-Level Waste in Opalinus Clay*, NAGRA Technical Report 09-02 (2009), www.nagra.ch.

3. L. Johnson and F. King, "The Effect of the Evolution of Environmental Conditions on the Corrosion Evolutionary Path in a Repository for Spent Fuel and High-Level Waste in Opalinus Clay," *Journal of Nuclear Materials* 379 (2008): 9–15, https://doi.org/10.1016/j.jnucmat.2008.06.003.

4. F. King and C. Padovani, "Review of the Corrosion Performance of Selected Canister Materials for Disposal of UK HLW and/or Spent Fuel," *Corrosion Engineering, Science and Technology* 46 (2011): 82–90, https://doi.org/10.1179/1743278211Y.0000000005.

5. F. King, "Comprehensive Nuclear Materials," in *Chapter 5.17: Waste Containers*, ed. R. J. M. Konings (Elsevier, 2012), 421–450, https://doi.org/10.1016/B978-0-08-056033-5.00131-2.

6. D. W. Shoesmith, "Assessing the Corrosion Performance of High-Level Nuclear Waste Containers," *Corrosion* 62 (2006): 703–722, https://doi.org/10.5006/1.3278296.

7. F. King, "Nuclear Waste Canister Materials: Corrosion Behavior and Long-Term Performance in Geological Repository Systems" in *Chapter 13*, *Geological Repository Systems for Safe Disposal of Spent Nuclear Fuels and Radioactive Waste*, 2nd ed. M. J. Apted and J. Ahn (Woodhead Publishing, 2017), 365–408, https://doi.org/10.1016/B978-0-08-100642-9.00013-X.

8. A. M. Beccaria and G. Poggi, "Influence of Hydrostatic Pressure on Pitting of Aluminium in Sea Water," *British Corrosion Journal* 20 (1985): 183–186, https://doi.org/10.1179/000705985798272632.

9. Z. Yang, B. Kan, J. Li, L. Qiao, A. A. Volinsky, and Y. Su, "A Statistical Study on the Effect of Hydrostatic Pressure on Metastable Pitting Corrosion of X70 Pipeline Steel," *Materials* 10 (2017): 1307, https://doi.org/10.3390/ma10111307.

10. H. Sun, L. Liu, Y. Li, and F. Wang, "Effect of Hydrostatic Pressure on the Corrosion Behavior of a Low Alloy Steel," *Journal of the Electrochemical Society* 160 (2013): C89–C96, https://doi.org/10.1149/2.040303jes.

11. Q. S. Li, S.-Z. Luo, X.-T. Xing, et al., "Effect of Deep Sea Pressures on the Corrosion Behavior of X65 Steel in the Artificial Seawater," *Acta Metallurgica Sinica (English Letters)* 32 (2019): 972–980, https://doi.org/10.1007/s40195-018-0856-8.

12. Z. X. Yang, B. Kan, J. X. Li, Y. J. Su, and L. J. Qiao, "Hydrostatic Pressure Effects on Corrosion Behavior of X70 Pipeline Steel in a Simulated Deep-Sea Environment," *Journal of Electroanalytical Chemistry* 822 (2018): 123–133, https://doi.org/10.1016/j.jelechem.2018.05.010.

13. C. Xu, Y. Zhu, W. Liu, et al., "Hydrostatic Pressure Effects on Corrosion Behaviour of X80 Steel in Artificial Sea Water," *Corrosion Engineering, Science and Technology* 56 (2021): 383–391, https://doi.org/10.1080/1478422X.2020.1866844.

14. X. Xiong, X. Ban, Y. Yan, and Y. Su, "Hydrostatic Pressure Effect on Double Layer Capacity of Iron," *Journal of Electroanalytical Chemistry* 871 (2020): 114306, https://doi.org/10.1016/j.jelechem.2020.114306.

15. R. Liu, Y. Cui, L. Liu, and F. Wang, "Study on the Mechanism of Hydrostatic Pressure Promoting Electrochemical Corrosion of Pure Iron in 3.5% NaCl Solution," *Acta Materialia* 203 (2021): 116467, https://doi.org/10.1016/j.actamat.2020.11.009.

16. X. L. Xiong, H. X. Ma, X. Tao, et al., "Hydrostatic Pressure Effects on the Kinetic Parameters of Hydrogen Evolution and Permeation in Armco Iron," *Electrochimica Acta* 255 (2017): 230–238, https://doi.org/10.1016/j.electacta.2017.09.181.

17. X. L. Xiong, Y. Xiang, J. X. Li, Y. J. Su, Q. J. Zhou, and A. A. Volinsky, "Hydrostatic Pressure Effects on Hydrogen Entry Into A514 Steel With Cathodic Deposits," *Electrochimica Acta* 283 (2018): 1534–1542, https://doi.org/10.1016/j.electacta.2018.07.049.

18. R. E. Melchers, "Effect of Immersion Depth on Marine Corrosion of Mild Steel," *Corrosion* 61 (2005): 895–906, https://doi.org/10.5006/1.3280659.

19. J. W. Muylder, "*Thermodynamics of Corrosion* in Comprehensive Treatise of Electrochemistry," in *Electrochemical Materials Science*, ed. J. O.′ M. Bockris, B. E. Conway, E. Yeager, and R. E. White (Springer Science, 1981) 4, https://doi.org/10.1007/978-1-4757-4825-3.

20. R. Hesse, M. Weiß, R. Szargan, P. Streubel, and R. Denecke, "Improved Peak-Fit Procedure for XPS Measurements of Inhomogeneous Samples—Development of the Advanced Tougaard Background Method," *Journal of Electron Spectroscopy and Related Phenomena* 205 (2015): 29–51, https://doi.org/10.1016/j.elspec.2015.06.013.

21. ASM Handbook Committee, Properties and Selection: Irons, Steels, and High-Performance Alloys 1 (ASM International, 1990).

22. S. Vazehrad, J. Elfsberg, and A. Diószegi, "Study of Microstructure and Silicon Segregation in Cast Iron Using Color Etching and Electron Microprobe Analysis," *Materials Characterization* 104 (2015): 132–138, https://doi.org/10.1016/j.matchar.2014.09.008.

23. J. Lacaze, J. Sertucha, and L. M. Åberg, "Microstructure of As-Cast Ferritic-Pearlitic Nodular Cast Irons," *ISIJ International* 56 (2016): 1606–1615, https://doi.org/10.2355/isijinternational.ISIJINT-2016-108.

24. R. P. Gupta and S. K. Sen, "Calculation of Multiplet Structure of Core P-Vacancy Levels," *Physical Review B* 10 (1974): 71–77, https://doi.org/10.1103/PhysRevB.10.71.

25. A. P. Grosvenor, B. A. Kobe, M. C. Biesinger, and N. S. McIntyre, "Investigation of Multiplet Splitting of Fe 2p XPS Spectra and Bonding in Iron Compounds," *Surface and Interface Analysis* 36 (2004): 1564–1574, https://doi.org/10.1016/j.actamat.2020.11.009.

26. A. Jablonski and C. J. Powell, "The Electron Attenuation Length Revisited," *Surface Science Reports* 47 (2002): 33–91, https://doi.org/10.1016/S0167-5729(02)00031-6.

27. R. T. Sanderson, "Principles of Electronegativity Part I. General Nature," *Journal of Chemical Education* 65 (1988): 112–118, https://doi.org/10.1021/ed065p112.

28. R. T. Sanderson, "Principles of Electronegativity Part II. Applications," *Journal of Chemical Education* 65 (1988): 227–231, https://doi.org/10.1021/ed065p227.

29. N. S. McIntyre and D. G. Zetaruk, "X-Ray Photoelectron Spectroscopic Studies of Iron Oxides," *Analytical Chemistry* 49 (1977): 1521–1529, https://doi.org/10.1021/ac50019a016.

30. NIST X-Ray Photoelectron Spectroscopy Database, NIST Standard Reference Database Number 20, National Institute of Standards and Technology, Gaithersburg MD, 20899 (2000), https://doi.org/10.18434/T4T88K.

31. V. P. Zakaznova-Herzog, H. W. Nesbitt, G. M. Bancroft, J. S. Tse, X. Gao, and W. Skinner, "High-Resolution Valence-Band XPS Spectra of the Nonconductors Quartz and Olivine," *Physical Review B* 72 (2005): 205113, https://doi.org/10.1103/PhysRevB.72.205113.

32. P. Guo and C. Wang, "Good Lithium Storage Performance of Fe_2SiO_4 as an Anode Material for Secondary Lithium Ion Batteries," *RSC Advances* 7 (2017): 4437–4443, https://doi.org/10.1039/C6RA26376C.

33. A. Alaoui-Mouayd, A. Koltsov, E. Sutter, and B. Tribollet, "Effect of Silicon Content in Steel and Oxidation Temperature on Scale Growth and Morphology," *Materials Chemistry and Physics* 143 (2014): 996–1004, https://doi.org/10.1016/j.matchemphys.2013.10.037.

34. A. R. Gonzalez-Elipe, J. P. Espinos, G. Munuera, J. Sanz, and J. M. Serratosa, "Bonding-State Characterization of Constituent Elements in Phyllosilicate Minerals by XPS and NMR," *Journal of Physical Chemistry* 92 (1988): 3471–3476, https://doi.org/10.1021/j100323a031.

35. W. Temesghen and P. Sherwood, "Analytical Utility of Valence Band X-Ray Photoelectron Spectroscopy of Iron and Its Oxides, With Spectral Interpretation by Cluster and Band Structure Calculations," *Analytical and Bioanalytical Chemistry* 373 (2002): 601–608, https://doi.org/10.1007/s00216-002-1362-3.

36. A. Lasia, "Hydrogen Evolution Reaction," in *Handbook of Fuel Cells: Fundamentals, Technology and Applications*, ed. W. Vielstich, A. Lamm, and H. A. Gasteiger (John Wiley & Sons, 2003), 416–440.

37. K. Takahashi, J. A. Bardwell, b MacDougall, and M. J. Graham, "Mechanism of Anodic Dissolution and Passivation of Iron—I. Behavior in Neutral Acetate Buffer Solutions," *Electrochimica Acta* 37 (1992): 477–487, https://doi.org/10.1016/0013-4686(92)87039-3.

38. D. R. MacFarlane and S. I. Smedley, "The Dissolution Mechanism of Iron in Chloride Solutions," *Journal of the Electrochemical Society* 133 (1986): 2240–2244, https://doi.org/10.1149/1.2108381.

39. S. Modiano, J. A. V. Carreño, C. S. Fugivara, et al., "Changes on Iron Electrode Surface During Hydrogen Permeation in Borate Buffer Solution," *Electrochimica Acta* 53 (2008): 3670–3679, https://doi.org/10.1016/j.electacta.2007.11.077.

40. T. Zakroczymski and J. Flis, "Impedance Characterization of the Activation of Iron Surface for Hydrogen Entry From Alkaline Solution," *Electrochimica Acta* 41 (1996): 1245–1250, https://doi.org/10.1016/0013-4686(95)00477-7.

41. S. Thomas, G. Sundararajan, P. D. White, and N. Birbilis, "The Effect of Absorbed Hydrogen on the Corrosion of Steels: Review, Discussion, and Implications," *Corrosion* 73 (2017): 426–436, https://doi.org/10.5006/2242.

42. R. Niu, H. Li, P.-Y. Liu, et al., "Hydrogen-Enhanced Deformation in Pearlite," *Acta Materialia* 281 (2024): 120327, https://doi.org/10.1016/j.actamat.2024.120327.

43. M. Kadowaki, I. Muto, K. Takahashi, et al., "Anodic Polarization Characteristics and Electrochemical Properties of Fe_3C in Chloride Solutions," *Journal of the Electrochemical Society* 166 (2019): C345–C351, https://doi.org/10.1149/2.1311912jes.

44. B. Hallstedt, D. Djurovic, J. von Appen, et al., "Thermodynamic Properties of Cementite (Fe_3C)," *Calphad* 34 (2010): 129–133, https://doi.org/10.1016/j.calphad.2010.01.004.

45. M. Pourbaix, *Atlas of Electrochemical Equilibria in Aqueous Solutions* (NACE, 1974).

46. E. Kim and K. Osseo-Asare, "Dissolution Windows for Hydrometallurgical Purification of Metallurgical-Grade Silicon to Solar-Grade Silicon: Eh–PH Diagrams for Fe Silicides," *Hydrometallurgy* 127–128 (2012): 178–186, https://doi.org/10.1016/j.hydromet.2012.05.013.

47. J.-P. Jolivet, C. Chanéac, and E. Tronc, "Iron Oxide Chemistry. From Molecular Clusters to Extended Solid Networks," *Chemical Communications (Cambridge, England)* 5 (2004): 481–487, https://doi.org/10.1039/B304532N.

48. J.-P. Jolivet, E. Tronc, and C. Chanéac, "*C.R.* Iron Oxides: From Molecular Clusters to Solid: A Nice Example of Chemical Versatility," *Geoscience* 6–7 (2006): 488–497, https://doi.org/10.1016/j.crte.2006.04.014.

49. J. Majzlan, C. B. Koch, and A. Navrotsky, "Thermodynamic Properties of Feroxyhyte (δ′-FeOOH)," *Clays and Clay Minerals* 56 (2008): 526–530, https://doi.org/10.1346/CCMN.2008.0560506.

50. P. Refait, C. Bon, L. Simon, et al., "Chemical Composition and Gibbs Standard Free Energy of Formation of Fe(II)-Fe(III) Hydroxysulphate Green Rust and Fe(II) Hydroxide," *Clay Minerals* 34 (1999): 499–510, https://doi.org/10.1180/000985599546280.

51. C. D. Wagner, D. E. Passoja, H. F. Hillery, et al., "Auger and Photoelectron Line Energy Relationships in Aluminum–Oxygen and Silicon–Oxygen Compounds," *Journal of Vacuum Science and Technology* 21 (1982): 933–944, https://doi.org/10.1116/1.571870.

52. T. L. Barr, "An XPS Study of Si as It Occurs in Adsorbents, Catalysts, and Thin Films," *Applications of Surface Science* 15 (1983): 1–35, https://doi.org/10.1016/0378-5963(83)90003-X.

53. P. C. M. Francisco, S. Mitsui, T. Ishidera, Y. Tachi, R. Doi, and H. Shiwaku, "Interaction of FeII and Si Under Anoxic and Reducing Conditions: Structural Characteristics of Ferrous Silicate Co-Precipitates," *Geochimica et Cosmochimica Acta* 270 (2020): 1–20, https://doi.org/10.1016/j.gca.2019.11.009.

54. R. Włodarczyk, J. Sauer, X. Yu, et al., "Atomic Structure of an Ultrathin Fe-Silicate Film Grown on a Metal: A Monolayer of Clay?," *Journal of the American Chemical Society* 135 (2013): 19222–19228, https://doi.org/10.1021/ja408772p.

55. Y. Qian, A. C. Scheinost, S. Grangeon, et al., "Oxidation State and Structure of Fe in Nontronite: From Oxidizing to Reducing Conditions," *ACS Earth and Space Chemistry* 7 (2023): 1868–1881, https://doi.org/10.1021/acsearthspacechem.3c00136.

Appendix

TABLE A1 | Parameters for the electrochemical kinetics of corrosion.

	Parameter	0.5 MPa	10 MPa
Water reduction	$k_{01}+$	10^{-5}	10^{-5}
	$k_{01}-$ $[OH^-]$	10^{-5}	10^{-15}
	α_1+	0.5	0.5
	$k_{02}+$	9.72×10^{-19}	7.77×10^{-16}
	α_2+	0.6	0.4
Iron dissolution	$k_{05}+$	10^{16}	4×10^{11}
	$k_{05}-$ $[H^+]$	10^{6}	40
	α_5+	0.5	0.3
	$k_{06}+$	2.22×10^{-6}	1.11×10^{-6}
	α_6+	0.15	0.2